nature communications

Article

https://doi.org/10.1038/s41467-026-69281-8

# Urea photosynthesis over a MOF-on-MOF S-scheme heterojunction

Received: 11 July 2025

Accepted: 28 January 2026

Published online: 06 February 2026

Check for updates

Yamin Xi[1], Chaoqi Zhang[1], Tong Bao[1], Suzhao Liu[1], Tianxiang Wang[1], Wenjing Tu[1], Yuntian Guo[1], Yingying Zou[1], Chengzhong Yu[1,2,3] & Chao Liu[1,2,4]

Photocatalytic nitrate reduction reaction coupled carbon dioxide reduction reaction holds great promise for sustainable urea synthesis, the design of photocatalysts with efficient C-N coupling and charge separation is crucial yet challenging. Herein, we report the synthesis of a novel MOF-on-MOF S-scheme heterojunction photocatalyst with interfacial dual active sites for efficient urea production via nitrate reduction reaction coupled carbon dioxide reduction reaction. The integration of semiconducting Zr-MOF and Co-MOF produces interfacial Co and Zr dual sites for $NO_3^-$ activation and $CO_2$ adsorption, synergistically promoting C-N coupling with reduced energy barriers. Besides, the S-scheme heterojunction enables the strong redox capability and facilitates the charge transfer. Consequently, the rationally designed MOF-on-MOF heterojunction achieves a high urea yield of 3523.4 μg $g^{-1}$ $h^{-1}$ and an apparent quantum yield of 1.16% at 365 nm in the absence of sacrificial agents. This work paves the way for the development of high-performance photocatalysts for urea production.

Urea ($CO(NH_2)_2$) serves as the most widely used nitrogen fertilizer in agriculture and a vital feedstock for chemical production[1–3]. The industrial urea production is primarily based on the Bosch-Meiser process by the reaction of ammonia ($NH_3$) and carbon dioxide ($CO_2$) under harsh conditions (150 °C–200 °C, 150–250 bar), which consumes large amounts of fossil fuels and emits substantial $CO_2$[4–7]. Photocatalytic $N_2$ and $CO_2$ co-reduction (PNRR&CRR) offers an ambient and sustainable alternative approach for urea production by using sunlight as the energy input, $N_2$, $CO_2$ and $H_2O$ as the raw materials[8,9]. However, the efficiency of PNRR&CRR remains unsatisfactory with urea yields lower than 1500 μg $h^{-1}$ $g_{cat}^{-1}$ in pure water, possibly ascribed to the low solubility of $N_2$ and high dissociation energy of N ≡ N bond (941 kJ $mol^{-1}$)[10,11].

Compared with inert $N_2$, nitrate ($NO_3^-$) is more active with lower N = O cleavage energy (204 kJ $mol^{-1}$) and higher aqueous solubility[11,12]. Substituting $N_2$ with $NO_3^-$ to couple with $CO_2$ is energetically more favorable for urea photosynthesis[13]. Besides, $CO_2$ is a common greenhouse gas and $NO_3^-$ is a widespread environmental pollutant in wastewater[14,15]. Photocatalytic co-reduction of $NO_3^-$ and $CO_2$ (P-NitRR&CRR) thus represents a promising strategy for simultaneous environmental remediation and value-added chemical production. Even the NitRR&CRR route has been reported in the field of electrocatalysis[16,17], the alternative P-NitRR&CRR route is hardly achieved. There is only report that delivered a urea production yield of just 0.22 μg $h^{-1}$ $g_{cat}^{-1}$ using $Cs_2CuBr_4/TiO_x$-Ar as the photocatalyst[13]. The development of high-performance photocatalysts to drive P-NitRR&CRR for urea synthesis remains a critical challenge.

As an important class of porous crystalline materials, metal-organic frameworks (MOFs) hold great promise as efficient photocatalysts owing to their large specific surface areas, high porosities and organic light-harvesting units, ligand-metal charge transfer pathway, as well as high tunability in compositions and structures[13,18,19]. Even MOFs photocatalysts have been extensively investigated, their application in photocatalytic urea synthesis remains unexplored.

[1]School of Chemistry and Molecular Engineering, East China Normal University, Shanghai, P. R. China. [2]State Key Laboratory of Petroleum Molecular and Process Engineering, SKLPMPE, East China Normal University, Shanghai, P. R. China. [3]Australian Institute for Bioengineering and Nanotechnology, The University of Queensland, Brisbane, QLD, Australia. [4]Shanghai Frontiers Science Center of Molecule Intelligent Syntheses, School of Chemistry and Molecular Engineering, East China Normal University, Shanghai, P. R. China. e-mail: cliu@chem.ecnu.edu.cn

Compared with traditional MOFs, construction of MOF-on-MOF heterostructures as heterojunction photocatalysts represents an emerging strategy for further improving the photocatalytic properties by enhancing light absorption, promoting charge separation and offering additional interfacial active sites[19]. To date, MOF-on-MOF photocatalysts have demonstrated promising potentials in the fields of $N_2$ fixation[19], water splitting[20], $CO_2$ reduction[21] and pollutant degradation[22], however the design of such photocatalysts for urea synthesis via the P-NitRR&CRR strategy has not been reported.

Herein, we report a MOF-on-MOF S-scheme heterojunction photocatalyst with interfacial dual active sites for efficient P-NitRR&CRR to urea production (Fig. 1). By growing Co-HHTP (HHTP = 2,3,6,7,10,11-hexahydroxytripehenylene) on NU-1000 (NU = Northwestern University), NU-1000@Co-HHTP is formed (Fig. 1a) with a S-scheme heterojunction (Fig. 1b) and interfacial Zr-Co dual active sites (Fig. 1c). The Co sites facilitate the reduction of $NO_3^-$ to *NO intermediates, while the Zr sites adsorb $CO_2$ for subsequent C-N coupling with *NO on neighboring Co sites, lowering the energy barrier for the generation of key C-N coupling intermediates. Further combined with the facilitated charge separation and strong redox capability of S-scheme heterojunction (Fig. 1b), the elaborately designed NU-1000@Co-HHTP photocatalyst exhibits a urea yield rate of 3523.4 $\mu g\ g^{-1}\ h^{-1}$ and an apparent quantum yield (AQY) of 1.16% at 365 nm, competitive with the reported photocatalysts.

## Results

The synthesis procedure of NU-1000@Co-HHTP heterostructure is schematically presented in Fig. 1a. Firstly, NU-1000 was prepared through a solvothermal reaction employing $ZrOCl_2{\cdot}8H_2O$ as metal sources and 4,4′,4″,4‴-(pyrene-1,3,6,8-tetrayl)tetrabenzoate ($H_4TBAPy$) as ligands[20,23]. The field-emission scanning electron microscope (SEM) and transmission electron microscopy (TEM) images of the resultant NU-1000 show a well-defined hexagonal rod-like morphology with smooth surface and solid nature (Supplementary Fig. 1a–c). The length and diameter are measure to be approximately 890 and 370 nm, respectively. The powder X-ray diffraction (XRD) pattern of NU-1000 (Supplementary Fig. 1d) matches well with the simulated crystal structure (CCDC 1580411)[24].

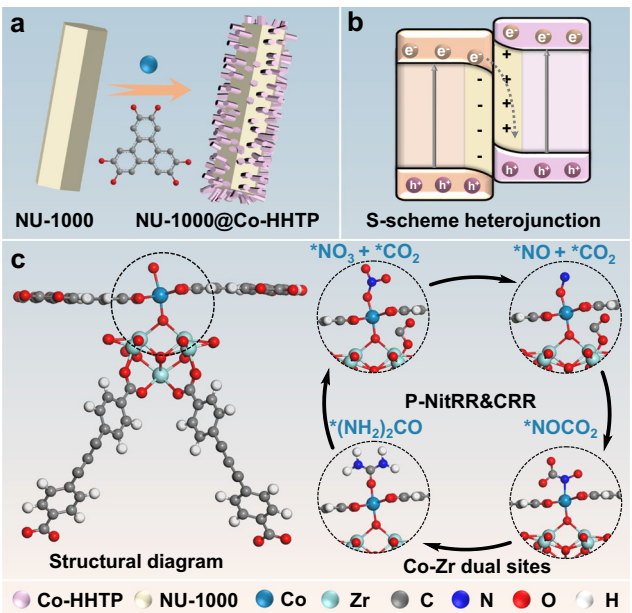


**Fig. 1 | Synthesis process and catalytic mechanism of NU-1000@Co-HHTP.** Illustration of **a** the synthesis process, **b** S-scheme heterojunction, and **c** P-NitRR&CRR mechanism of NU-1000@Co-HHTP. The dotted circles in (**c**) highlight the interfacial active sites for catalyzing P-NitRR&CRR.

By subsequent reaction of NU-1000 with $Co^{2+}$ and HHTP in 1-propanol solution, the NU-1000@Co-HHTP heterostructure was obtained[25]. The SEM image (Fig. 2a) of NU-1000@Co-HHTP exhibits uniform microrods with rough surface. At higher magnification (Fig. 2b), Co-HHTP nanorods with an average length of 71 nm and diameter of 39 nm are found densely adhered on the surface of NU-1000. From the SEM image of one broken particle (Supplementary Fig. 2) and the TEM image (Fig. 2c), the formation of rod-on-rod core-shell heterostructure is clearly demonstrated. Figure 2d displays the HRTEM image collected from a single nanorod on the shell. The lattice fringes with a d-spacing of 1.91 nm (indicated by the yellow circle) correspond to the (100) plane of crystalline Co-HHTP[26]. The spatial elemental distribution was then examined by energy dispersive X-ray (EDX) spectroscopy. The high-angle annular dark-field scanning transmission electron microscopy (HAADF-STEM) and elemental mapping images as well as the line scanning spectra of NU−1000@Co-HHTP are shown in Fig. 2e, f. The signals of C and O elements are evenly detected throughout the whole particle, while those of Zr and Co elements are predominately distributed in the internal core and external shell regions, respectively, further verifying the core-shell heterostructure of NU−1000@Co-HHTP. Moreover, the Co and Zr mass ratio of NU-1000@Co-HHTP was measured to be 13.02% and 8.29%, respectively, via inductively coupled plasma-optical emission spectrometry (ICP-OES, Supplementary Table 1). The Zr/Co molar ratio was thus calculated to be 10.11:10.00, corresponding to a NU-1000/Co-HHTP mass ratio of 1.25/1.00.

To investigate the crystalline and chemical structures of NU-1000@Co-HHTP, XRD and Fourier-transform infrared (FTIR) spectroscopy analyses were performed. In addition to NU-1000, Co-HHTP nanorods (Supplementary Fig. 3) were also prepared as a control sample by using the similar synthesis protocol of NU-1000@Co-HHTP without the addition of NU-1000. The mass ratios of Co and Zr of Co-HHTP and NU-1000 were determined as 18.66% and 23.44%, respectively, close to the theoretical values. As shown in Fig. 2g, h, the characteristic diffraction peaks of both NU-1000 and Co-HHTP are detected in the XRD pattern of NU-1000@Co-HHTP. In the FTIR spectrum of NU-1000@Co-HHTP (Supplementary Fig. 4), the bands at 1603, 1412 and 783, 712, 664 $cm^{-1}$ are attributed to the $\nu_{as}$(-$COO^-$), $\nu_s$(-$COO^-$) and Zr-O vibration of NU-1000, respectively[26]. Besides, the peaks assigned to the benzene skeleton vibrations of Co-HHTP are also observed at 1454, 1365, and 1215 $cm^{-1}$[27]. In addition, the peak of adsorbed $H_2O$ is also found at 1655 $cm^{-1}$.

$N_2$ sorption analysis (Fig. 2i) was used to characterize the textural properties of NU-1000, Co-HHTP and NU-1000@Co-HHTP. The $N_2$ sorption isotherm of Co-HHTP shows a type I hysteresis loop with microporous nature. Different from Co-HHTP, NU-1000 and NU-1000@Co-HHTP exhibit a micro-mesopore coexisting structure[28]. The Brunauer-Emmett-Teller (BET) specific surface areas of NU-1000, Co-HHTP and NU-1000@Co-HHTP are calculated to be 1150.1, 322.78, and 933.42 $m^2\ g^{-1}$, with corresponding pore volumes of 0.86, 0.43, and 0.75 $cm^3 g^{-1}$, respectively (Supplementary Table 2). From the pore size distribution curve of NU-1000@Co-HHTP, both micropores of 1.12 nm from Co-HHTP and mesopores of 2.30 nm originated from NU-1000 are observed (Supplementary Fig. 5). The above results demonstrate the successful fabrication of NU-1000@Co-HHTP heterostructures.

The electronic structure and coordination environment of the samples were investigated using X-ray absorption near-edge structure (XANES) and extended X-ray absorption fine structure (EXAFS) analysis. As shown in Fig. 3a, the Co K-edge absorption for NU-1000@Co-HHTP exhibits an increased edge energy than that for Co-HHTP. In contrast, the Zr K-edge position for NU-1000@Co-HHTP negatively shifts compared to that for NU-1000. The observations suggest the electron transfer from Co-HHTP to NU-1000 within NU-1000@Co-

https://doi.org/10.1038/s41467-026-69281-8

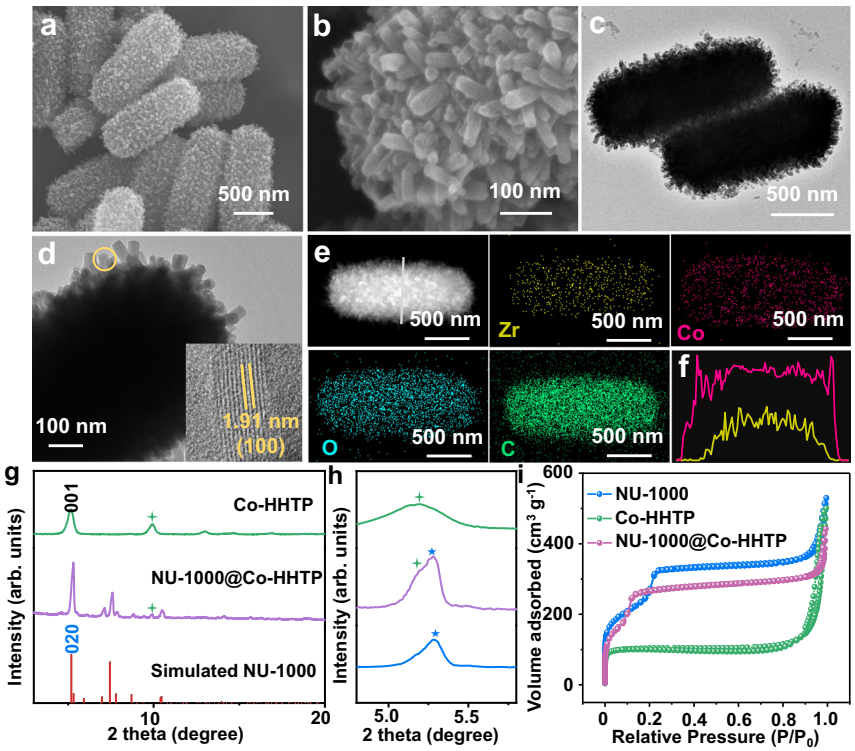


**Fig. 2 | Morphology and structural characterization. a**, **b** SEM, **c**, **d** TEM, **e** HADDF-STEM and element mapping images, and **f** line scanning elemental distribution profile collected along the white line in (**e**) of NU-1000@Co-HHTP. **g** XRD patterns, **h** locally enlarged pattern of (**g**), and (**i**) $N_2$ sorption isotherms of NU-1000, Co-HHTP and NU-1000@Co-HHTP. The inset in (**d**) shows a HRTEM image of Co-HHTP recorded in the region marked by yellow circle. Source data for Fig. 2 are provided as a Source Data file.

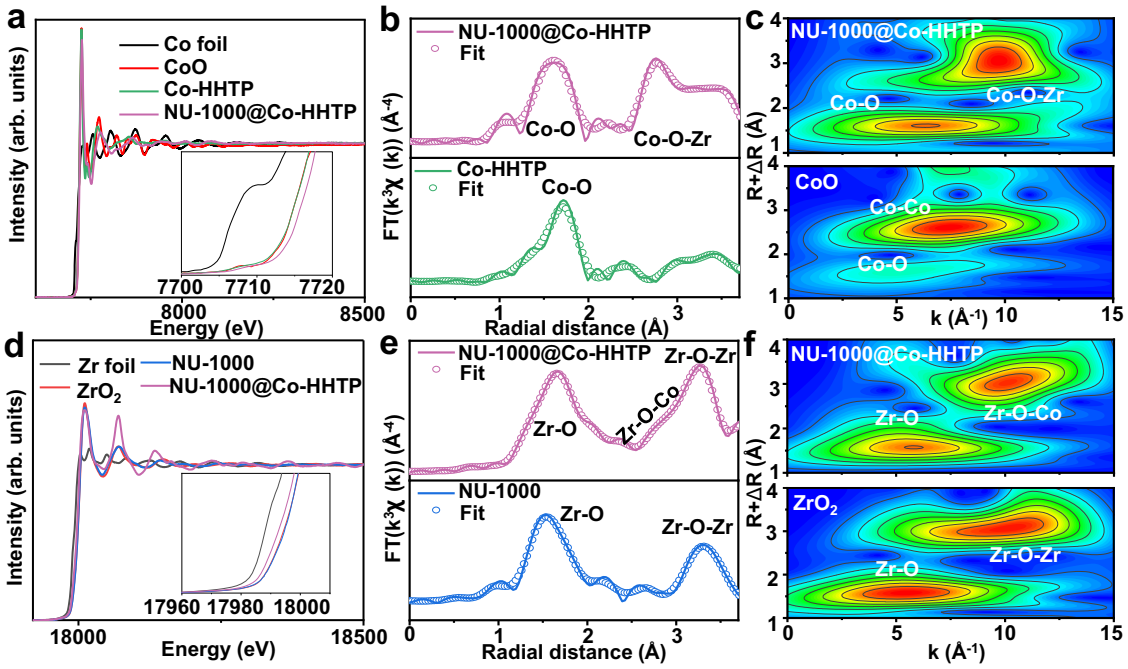


**Fig. 3 | Electronic structure characterization. a** Co K-edge and **d** Zr K-edge XANES spectra of different samples. Insets in (**a**) and (**d**) are magnified images. **b** Co K-edge and **e** Zr K-edge FT-EXAFS spectra of different samples. Wavelet transforms for **c** Co and **f** Zr K-edge EXAFS. Source data for Fig. 3 are provided as a Source Data file.

HHTP, resulting in the generation of electron deficient Co and electron-sufficient Zr sites. In the Co K-edge Fourier transform (FT) EXAFS spectra (Fig. 3b, Supplementary Table 3), the characteristic peak at 1.71 Å is assigned to Co-O coordination between Co and HHTP ligands in Co-HHTP. For NU-1000@Co-HHTP, apart from the Co-O bond, a distinct peak attributed to the Co-O-Zr bond emerges at 2.75 Å (Fig. 3b). Figure 3e displays the Zr K-edge spectrum of NU-1000, where the peaks located at around 1.51 and 3.29 Å correspond to the Zr-O and

https://doi.org/10.1038/s41467-026-69281-8

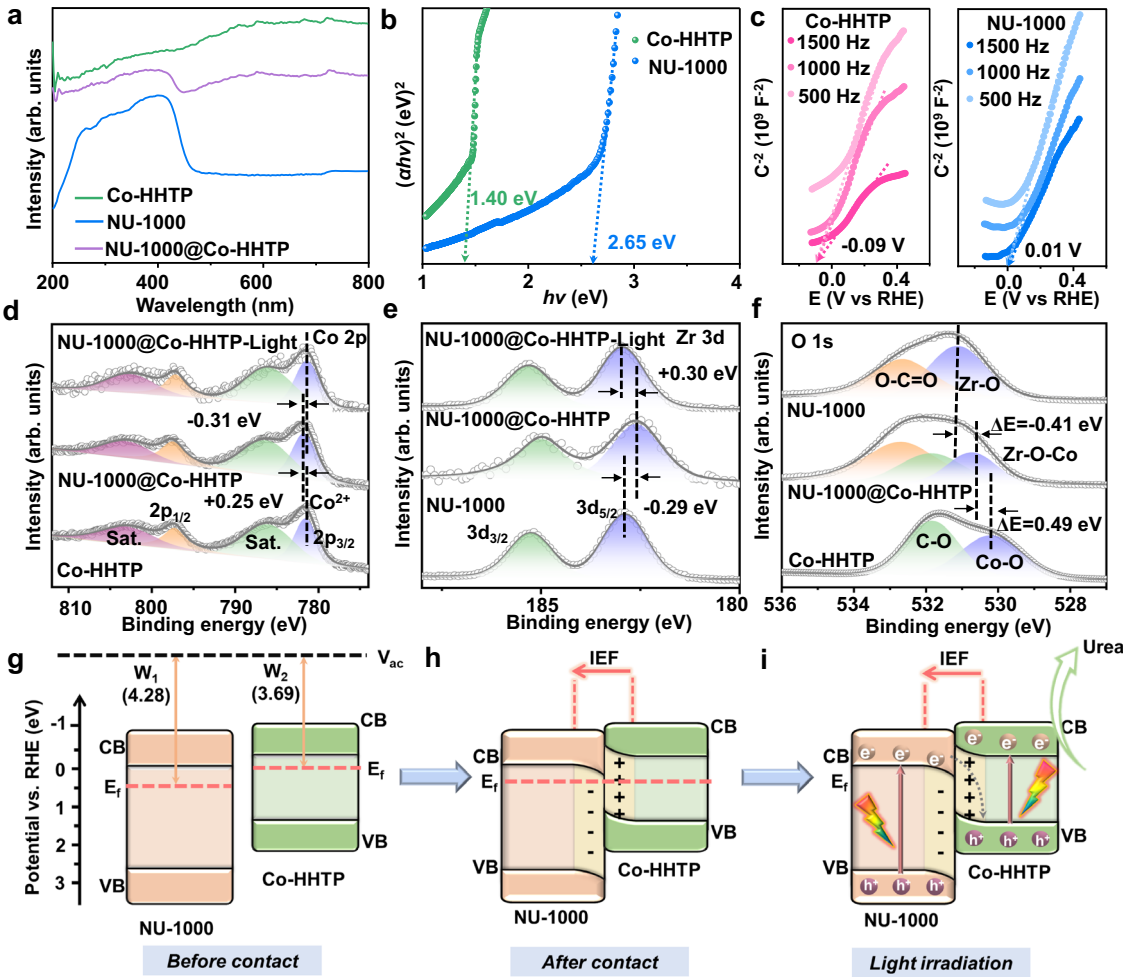


**Fig. 4 | Energy band structure and charge transfer mechanism. a** UV-vis DRS spectra of NU-1000, Co-HHTP, NU-1000/Co-HHTP, NU-1000@Co-HHTP, **b** Tauc plots and **c** Mott-Schottky plots of NU-1000 and Co-HHTP, XPS spectra of **d** Co 2*p*, **e** Zr 3*d* and **f** O 1*s* of NU-1000, Co-HHTP and NU-1000@Co-HHTP, **g**–**i** schematic illustration of the S-scheme charge transfer mechanism of NU-1000@Co-HHTP. The dash lines and arrows in (**d**–**f**) indicates the binding energy shift of Co 2*p*, Zr 3*d* and O 1*s* peaks. Source data for Fig. 4 are provided as a Source Data file.

Zr-O-Zr bond, respectively. For NU-1000@Co-HHTP, an additional peak of Zr-O-Co bond is found at ≈2.77 Å, in accordance with the results of Co K-edge spectra. Compared to the Zr-O-Zr bond, the shorter bond length of Zr-O-Co is attributed to the smaller radius of Co than Zr. Moreover, the derived wavelet transform diagrams (Fig. 3c, f) offer visual evidence for the formation of Zr-O-Co chemical bonds at the NU-1000@Co-HHTP heterointerface.

The optical properties and electronic band structures of the samples were explored by ultraviolet-visible diffuse reflectance spectroscopy (UV-vis DRS) and Mott-Schottky analysis. From the UV-vis DRS spectra and corresponding Tauc plots (Figs. 4a and 4b), NU-1000 exhibits an absorption edge at 460 nm with a bandgap ($E_g$) of 2.65 eV, close to the reported results[29]. After combination with Co-HHTP with a narrower bandgap of 1.40 eV, NU-1000@Co-HHTP shows significantly enhanced light absorption intensity than NU-1000 from UV to near-infrared region. Figure 4c shows the Mott-Schottky curves of NU-1000 and Co-HHTP at the frequencies of 500, 1000, and 1500 Hz. The positive slopes of two samples reflect their n-type semiconductor features[29]. Based on the transverse intercept values, the flat-band potentials of NU-1000 and Co-HHTP were determined to be 0.01 and -0.09 V, respectively. For n-type semiconductors, the conduction band (CB) position is typically ~0.1 eV below the flat-band potential[30,31]. Therefore, the CB potentials of NU-1000 and Co-HHTP are calculated to be -0.09 and -0.19 V (vs RHE), respectively.

X-ray photoelectron spectroscopy (XPS) was applied for unveiling the charge transfer between NU-1000 and Co-HHTP within NU-1000@Co-HHTP heterostructure. In addition to NU-1000 and Co-HHTP, a physically mixed NU-1000/Co-HHTP sample was also prepared as comparison. The full survey spectrum of NU-1000@Co-HHTP (Supplementary Fig. 6) reveals the presence of Zr, Co, O and C elements, consistent with the element mapping observations. The high-resolution XPS spectra of Co 2*p*, Zr 3*d* and O 1*s* collected without irradiation are shown in Fig. 4d–f. The Co 2*p* spectrum of Co-HHTP (Fig. 4d) could be deconvoluted into Co $2p_{3/2}$ and $2p_{1/2}$ peaks of $Co^{2+}$ at 781.53 and 797.13 eV, and two satellite peaks at 786.09 and 802.79 eV, respectively. By integrating with NU-1000, the binding energies of Co 2*p* peaks for NU-1000@Co-HHTP increase by 0.25 eV, corresponding to the decreased electron density of Co. The Zr 3*d* spectrum of NU-1000 presents two distinct peaks at 182.89 and 185.24 eV, attributed to Zr $3d_{5/2}$ and Zr $3d_{3/2}$, respectively. In opposite to Co, the Zr 3*d* peaks of NU-1000@Co-HHTP exhibit a negative shift of ≈0.29 eV, manifesting the electron transfer from Co in Co-HHTP to Zr in NU-1000. The O 1*s* spectrum of NU-1000 is displayed in Fig. 4f, which can be fitted into two peaks of O-C = O group and Zr-O bond at 532.67 and 531.14 eV, respectively. For Co-HHTP, the two peaks at 531.85 and 530.24 eV

belong to the C-O group and Co-O bond, respectively. The combination of the two components generates a distinct peak at 530.73 eV in the spectrum of NU-1000@Co-HHTP, positioned between Co-O peak of Co-HHTP and Zr-O peak of NU-1000, suggesting the formation of Zr-O-Co chemical bonds at the NU-1000/Co-HHTP interface[22,32]. In contrast to the significant variations in binding energies of the elements observed in NU-1000@Co-HHTP, the electron states of Co and Zr in NU-1000/Co-HHTP exhibit negligible changes compared to NU-1000 and Co-HHTP, suggesting the more intimate interfacial contact between the two components in NU-1000@Co-HHTP.

To elucidate the electron transfer of NU-1000@Co-HHTP under visible-light illumination, in situ irradiated XPS (ISIXPS) measurement was further carried out. Compared to the spectra in darkness, the binding energies of Co 2*p* peaks in the ISIXPS spectrum decrease by 0.31 eV (Fig. 4d), while those of Zr 3*d* peaks present a positive shift of 0.3 eV. The observations indicate the transportation of photogenerated electrons from NU-1000 to Co-HHTP under light irradiation. Subsequently, ultraviolet photoelectron spectroscopy (UPS) was employed to measure the work function ($\Phi$) and Fermi levels ($E_f$) of NU-1000 and Co-HHTP. Supplementary Fig. 8 shows the UPS spectra measured at -10 V bias, where the $\Phi$ values of NU-1000 and Co-HHTP were determined to be 4.38, and 3.99 eV, respectively, using the formula of $\Phi = hv - (E_{cutoff} - E_{fermi})$, where $E_{cutoff}$ and $E_{fermi}$ represent the secondary electron cutoff and Fermi edge, respectively. Subsequently, the $E_f$ values of NU-1000 and Co-HHTP were calculated to be -4.38 and -3.99 eV (vs vacuum level), respectively, according to the formula of $\Phi = E_v - E_f$ ($E_v = 0$)[33]. Further based on UPS measurements performed without external bias (Supplementary Fig. 9), the valence band maximum (VBM) positions were determined to be 6.60 eV for NU-1000 and 5.23 eV for Co-HHTP using the equation of $E_{VB} = 21.22 - (E_{cut\ off} - E_{Fermi} - E_{cut\ on})$[20]. Then, the VB potentials relative to NHE are calculated as 2.57 V for NU-1000 and 1.20 V for Co-HHTP according to the formula of $E_{VB}$ (vs. RHE) = $E_{VB} - 4.03$, well matching with the values measured by Mott–Schottky diagrams and Tauc plots. Besides, valence band XPS (VB-XPS) measurement was performed to further analyze the valance band of the samples. Based on the VB-XPS spectra (Supplementary Fig. 10), the VB values of NU-1000 and Co-HHTP were determined as 2.58 and 1.22 V (vs. RHE), respectively. In combination with the results of Mott–Schottky diagrams and Tauc plots, the band structures of NU-1000 and Co-HHTP are depicted in Fig. 4g.

Based on the UV-vis DRS, Mott-Schottky, XPS and UPS results, the charge transfer mechanism within the NU-1000@Co-HHTP heterojunction is postulated. As the energy band structures (Fig. 4g) reveals higher band positions and $E_f$ of Co-HHTP than NU-1000. Upon contact to form a heterojunction, the free electrons in Co-HHTP are transferred to NU-1000 until the $E_f$ equilibrium is reached, leading to an internal electric field (IEF) pointing from Co-HHTP to NU-1000 at the interface (Fig. 4h). Driven by the IEF, the bands of Co-HHTP and NU-1000 bend upward and downward, respectively. Under illumination, electrons are excited from the VB of Co-HHTP and NU-1000 to their CB, leaving photogenerated holes in the VB. Subsequently, the IEF and band bending facilitates the migration of photogenerated electrons in CB of NU-1000 to VB of Co-HHTP with the photogenerated holes consumed (Fig. 4i). Consequently, the photogenerated electrons and holes are accumulated in CB of Co-HHTP and VB of NU-1000 with maximumly preserved redox capability. The charge transfer manner of NU-1000@Co-HHTP heterojunction well aligns with the S-scheme mechanism[34].

The photocatalytic performance of urea synthesis via co-reduction of $NO_3^-$ and $CO_2$ was evaluated in a sealed quartz photoreactor system containing $CO_2$-saturated $NO_3^-$ aqueous solution (Supplementary Fig. 11). The yield of generated urea was quantified by colorimetric method and $^1$H nuclear magnetic resonance (NMR) spectroscopy (Supplementary Figs. 12 and 13). As shown in Fig. 5a and Supplementary Fig. 14, NU-1000@Co-HHTP with an optimized dosage of 0.5 mg mL$^{-1}$ delivers a urea production amount of 4.70 μmol within 4 h, exceeding NU-1000 (0.26 μmol), Co-HHTP (0.89 μmol) and NU-1000/Co-HHTP (0.59 μmol). Moreover, the urea production rate of NU-1000@Co-HHTP is calculated to be 3523.4 μg h$^{-1}$ g$^{-1}$ (Fig. 5b), ~18.4, 5.3 and 8-folds higher than that of NU-1000 (191.8 μg h$^{-1}$ g$^{-1}$), Co-HHTP (664.7 μg h$^{-1}$ g$^{-1}$) and NU-1000/Co-HHTP (440.9 μg h$^{-1}$ g$^{-1}$), respectively, indicating the enhanced photocatalytic activity of NU-1000@Co-HHTP. Furthermore, quantitative $^1$H NMR analysis indicates that the urea yield is consistent with the result obtained from the colorimetric method (Supplementary Fig. S15).

Except for urea, other possible byproducts including $NH_3$, $NO_2^-$, CO and $H_2$ were also detected by UV-Vis spectroscopy and gas chromatography (Fig. 5b, Supplementary Figs. S16 and S17). When catalyzed by NU-1000, CO is generated as the main byproduct with the highest yield of 853.2 μg h$^{-1}$ g$^{-1}$ among all samples. In contrast, Co-HHTP predominately produces $NH_3$ with a yield 727.6 μg h$^{-1}$ g$^{-1}$, higher than that of NU-1000 (195.2 μg h$^{-1}$ g$^{-1}$), NU-1000/Co-HHTP (242.4 μg h$^{-1}$ g$^{-1}$) and NU-1000@Co-HHTP (166.4 μg h$^{-1}$ g$^{-1}$). Besides, $NO_2^-$ is almost undetectable with only trace amounts of $H_2$ for all samples. Based on these results, it is speculated that NU-1000 and Co-HHTP mainly favor $CO_2$RR and $NO_3^-$RR, respectively. By integrating NU-1000 and Co-HHTP, the C-N coupling toward urea production over NU-1000@Co-HHTP is greatly promoted.

Except for the P-NitRR&CRR process, the coupled water oxidation reaction was also explored. As shown in Supplementary Fig. 18, the yield of $O_2$ as the oxidation product follows the order of NU-1000@Co-HHTP (962.3 μmol g$^{-1}$ h$^{-1}$) > Co-HHTP (213.2 μmol g$^{-1}$ h$^{-1}$) > NU-1000/Co-HHTP (184.9 μmol g$^{-1}$ h$^{-1}$) > NU-1000 (101.2 μmol g$^{-1}$ h$^{-1}$).

Afterwards, the apparent quantum yield (AQY) was examined to assess the light utilization efficiency under monochromatic light irradiation from 365 to 650 nm. As presented in Fig. 5c, the AQY of NU-1000@Co-HHTP exhibits a wavelength-dependent trend, in line with the absorption spectrum. A maximum AQY value of 1.16% is achieved at 365 nm (Fig. 5c, Supplementray Table 4). Both the urea yield and AQY of NU-1000@Co-HHTP are competitive with the reported photocatalysts used in both NRR&CRR and NitRR&CRR systems (Supplementary Table 5)[8,10,13,31,35–38]. Nevertheless, the performance of NU-1000@Co-HHTP-based P-NitRR&CRR system is inferior to the state-of-the-art electrocatalytic NitRR&CRR (E-NitRR&CRR) systems (Supplementary Table 6), inspiring further advances in the design of efficient photocatalysts and photocatalytic systems.

To study the urea formation pathway through $CO_2$ and $NO_3^-$ co-reduction, an isotopic labeling experiment was conducted. In the $^1$H NMR spectrum (Fig. 5d), the characteristic signals corresponding to $(^{15}NH_2)_2CO$ and $(^{14}NH_2)_2CO$ are detected when using $^{15}NO_3^-$ and $^{14}NO_3^-$ as the nitrogen source, respectively[38]. Upon changing the feeding gas to $^{13}CO_2$, a typical singlet peak of $^{13}CO(NH_2)_2$ is observed in the C NMR spectrum (Supplementary Fig. 19), indicating that the carbon in urea is derived from $CO_2$. In addition, almost no urea could be formed in the reaction systems with only $CO_2$ or $NO_3^-$, and without catalysts or light irradiation, verifying that urea is produced from P-NitRR&CRR (Fig. 5e). Except for activity, the catalytic stability of NU-1000@Co-HHTP was also explored. As shown in Fig. 5f, ≈97.3% of the original urea yield is preserved after ten consecutive reaction cycles with each cycle lasting for 4 h, suggesting the stability of NU-1000@Co-HHTP. Additionally, comparative characterizations of NU-1000@Co-HHTP before and after photocatalysis using SEM, TEM, XRD, FTIR and ICP (Supplementary Figs. 20, 21 and Table 7) reveal almost unchanged morphology, crystal structure and chemical composition. In the supernatant after reaction, only trace amounts of Co and Zr were detected (0.030 and 0.024 mg/L, respectively). The mass ratios of leached Co and Zr from NU-1000@Co-HHTP are thus estimated as 0.07% and 0.03%, respectively, further demonstrating the structural stability of NU-1000@Co-HHTP. Besides, the decreased intensity of

https://doi.org/10.1038/s41467-026-69281-8

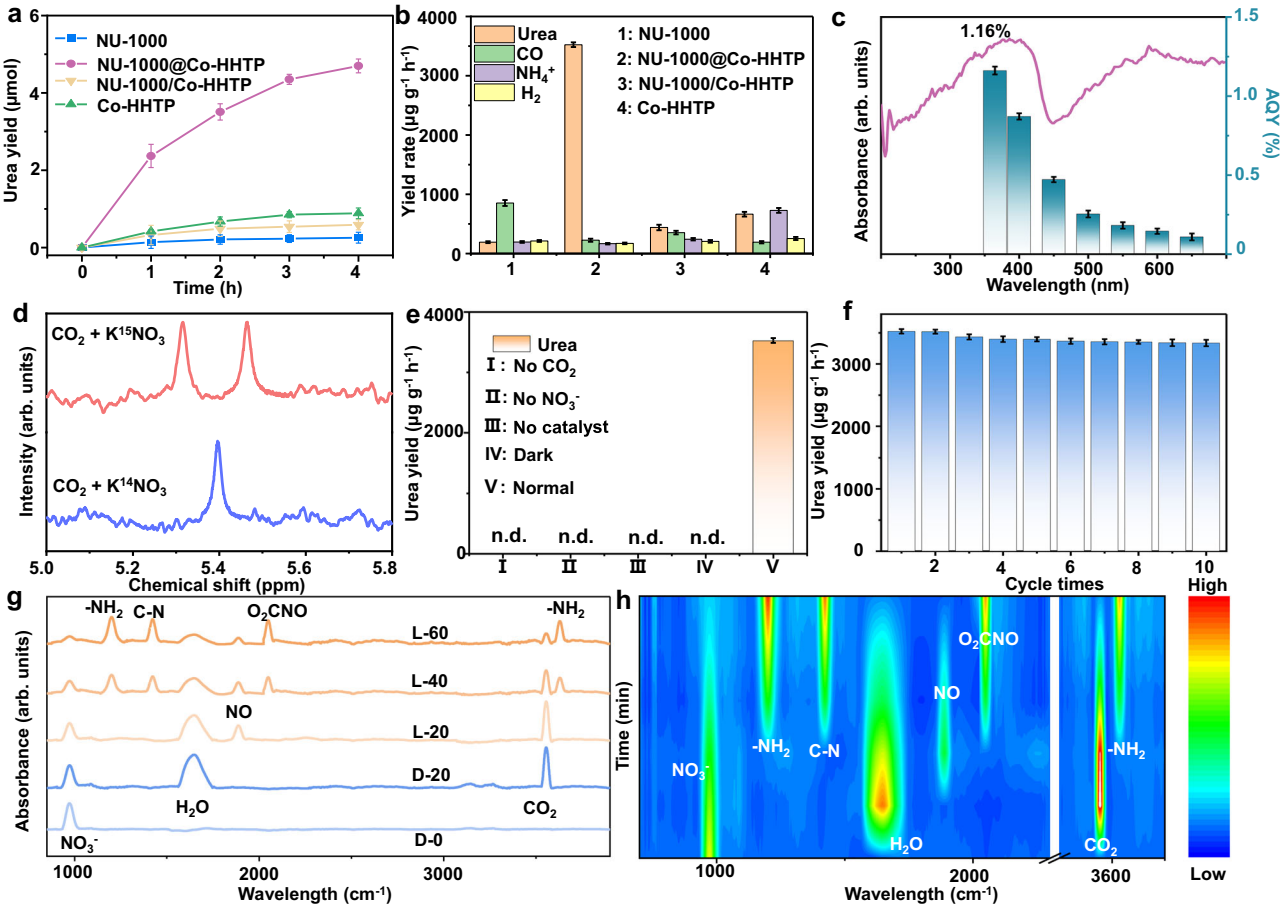


**Fig. 5 | Photocatalytic performance. a** Time courses of urea production for NU-1000, Co-HHTP, NU-1000/Co-HHTP and NU-1000@Co-HHTP, **b** yield rates of different products on NU-1000, Co-HHTP, NU-1000/Co-HHTP and NU-1000@Co-HHTP, **c** wavelength-dependent AQY of NU-1000@Co-HHTP, **d** $^{1}$H NMR spectra of urea generated by using $^{14}NO_3^-$ and $^{15}NO_3^-$ as the feedstocks, **e** photocatalytic urea production over NU-1000@Co-HHTP under different conditions, **f** urea yield rates of NU-1000@Co-HHTP during recycling stability test, in situ FTIR spectra and corresponding contour projections of **g**, **h** NU-1000@Co-HHTP, respectively. Error bars represent the standard error of the mean from three independent experimental measurements. Source data for Fig. 5 are provided as a Source Data file.

satellite peak of $Co^{2+}$ in the XPS spectrum may be caused by the increased oxidation state of Co sites by adsorbing $NO_3^-$ [39].

To unravel the mechanism of photocatalytic C-N coupling, in situ diffuse reflectance infrared Fourier transform spectroscopy (DRIFTS) was employed to monitor the reaction intermediates in real-time. The DRIFTS spectra and corresponding contour projection diagrams of NU-1000, Co-HHTP and NU-1000@Co-HHTP are shown in Supplementary Figs. 22, 24 and Fig. 5g, h. In the spectra of NU-1000@Co-HHTP collected in darkness, the peaks assigned to the adsorbed $CO_2$, $H_2O$ and $NO_3^-$ are observed at 3555, 1642 and 978 $cm^{-1}$, respectively[38,40–43]. Under light illumination for 20 min, the peak intensities of $NO_3^-$ and $H_2O$ are reduced with an additional peak of *NO intermediate generated at 1886 $cm^{-1}$[44]. At 40 min, the peaks of *NO and $CO_2$ are synchronously weakened, accompanied with the formation of $*O_2CNO$ at 2056 $cm^{-1}$, a key C-N coupling intermediate via the interaction between $CO_2$ and *NO[45]. Compared to the widely recognized *OCNO intermediate (~2075 $cm^{-1}$)[45], the peak of $*O_2CNO$ exhibits a red shift of ~19 $cm^{-1}$, which may be attributed to the lower C-N bond order of $*O_2CNO$ than that of *OCNO. In addition, other peaks attributed to the bending and wagging modes of -$NH_2$ (1206 and 3630 $cm^{-1}$) and stretching mode of C-N bond (1425 $cm^{-1}$) of urea also emerge[5,46,47]. By prolonging the reaction time to 60 min, the peak intensities of $CO_2$, $H_2O$, $NO_3^-$ and *NO further decrease while those of $*CO_2NO$ and urea are gradually intensified, indicating the continuous occurrence of P-NitRR&CRR toward urea production.

For NU-1000 (Supplementary Fig. 22a, b), the spectra collected under dark conditions also exhibit strong peaks of the three reactants. After irradiation of 60 min, the adsorbed $CO_2$ is largely consumed with only marginally reduced $NO_3^-$ peak. The peaks of $*O_2CNO$ intermediate and urea are much weaker than those of NU-1000@Co-HHTP. Moreover, the peak at 1460 $cm^{-1}$ belongs to the *CO intermediate, suggesting CO as the main byproduct from $CO_2$RR over NU-1000[48]. In addition, the absence of *CO signals in the in-situ DRIFTS spectra for NU-1000@Co-HHTP and Co-HHTP may be ascribed to the low $CO_2$ reduction activity and weak *CO adsorption at the Co sites, which result in undetectably low surface *CO concentrations[49–51]. The speculation is further supported by the CO temperature-programmed desorption (CO-TPD) measurement. As shown in Supplementary Fig. 23, the CO-TPD profile of NU-1000 exhibits two distinct peaks at 133 and 390 °C, assigned to the physisorption and chemisorption of CO, respectively. For Co-HHTP, both the physisorption and chemisorption temperature is significantly lower than that of NU-1000, along with reduced peak intensities, indicating weaker CO adsorption at Co sites of Co-HHTP than NU-1000. After forming heterojunction, the CO adsorption strength of NU-1000@Co-HHTP lies between that of the two individual components. In contrary to NU-1000 (Supplementary Fig. 24a, b), the photocatalytic reaction over Co-HHTP is dominated by NitRR to $NH_3$ (1301 $cm^{-1}$)[52,53]. The limited $CO_2$ adsorption and activation abilities result in the low C-N coupling efficiency. The evolution trend of

byproducts and products in in-situ DRIFTS spectra well match with the photocatalytic results.

Linear sweep voltammetry (LSV) method was employed to assess the $CO_2$ and $NO_3^-$ reduction activity of the samples. As shown in Supplementary Figs. 25 and 26a–c, the current densities of NU-1000@Co-HHTP in the presence of $NO_3^-$, $CO_2$ or both $NO_3^-$ and $CO_2$ are larger than that in 0.5 M $Na_2SO_4$ without reactants. Moreover, NU-1000 exhibits higher current densities than Co-HHTP in the $CO_2$-saturated $Na_2SO_4$ electrolyte (Supplementary Fig. 26a), whereas a reversed trend is observed in Ar-saturated $KNO_3$ electrolyte, indicating the predominated $CO_2$RR and NitRR process over NU-1000 and Co-HHTP, respectively. Upon forming heterojunction, both the $CO_2$ and $NO_3^-$ activation capabilities of NU-1000@Co-HHTP are enhanced compared to the individual materials. Moreover, in $CO_2$-saturated $KNO_3$ electrolyte, NU-1000@Co-HHTP exhibits a significantly lower onset potential and higher current density than NU-1000 and Co-HHTP, demonstrating facilitated co-reduction reaction of $CO_2$ and $NO_3^-$ for C-N coupling (Supplementary Fig. 26c).

Owing to the much lower solubility and diffusion efficiency of $CO_2$ compared to $NO_3^-$ in aqueous media, $CO_2$ adsorption capacity of catalysts has been recognized as a critical rate-limiting factor that governs the C-N coupling efficiency[14,54–56]. Therefore, $CO_2$ sorption and $CO_2$-TPD were further carried out to investigate the $CO_2$ adsorption behaviors on different samples. As shown in the $CO_2$ sorption isotherms (Supplementary Fig. 26d), NU-1000@Co-HHTP exhibit a $CO_2$ adsorption capacity of 44.76 $cm^3 g^{-1}$ at 273 K (Supplementary Table 8), locating between NU-1000 (68.43 $cm^3 g^{-1}$) and Co-HHTP (18.18 $cm^3 g^{-1}$). The $CO_2$-TPD profiles of NU-1000, Co-HHTP and NU-1000@Co-HHTP are presented in Supplementary Fig. 26e, where the peaks in the low-temperature region (<200 °C) and high-temperature (200-500 °C) refer to the physical and chemical adsorption of $CO_2$, respectively. The temperature and area of physisorption peak follows the order of NU-1000 > NU-1000@Co-HHTP > Co-HHTP, possibly ascribed to the largest specific surface area of NU-1000. The chemisorption temperature of NU-1000 is also higher than Co-HHTP but lower than NU-1000@Co-HHTP, suggesting the promoted $CO_2$ chemisorption by forming heterojunction. The results of photocatalysis tests, in-situ DRIFTS spectra, LSV curves, $CO_2$ sorption isotherms and $CO_2$-TPD spectra collaboratively reveal that NU-1000@Co-HHTP simultaneously integrates the strong $CO_2$ adsorption capability and NitRR activity, resultantly improving the C-N coupling efficiency for urea production.

Subsequently, the charge separation and transfer kinetics of the samples were examined by using photoelectrochemical (PEC) and photoluminescence (PL) measurements. As shown in Supplementary Figs. 26f and Fig. 27a, NU-1000@Co-HHTP has the highest transient photocurrent response and smallest arc radius among all samples, indicating its boosted charge separation efficiency. The fitted EIS spectra and corresponding equivalent circuit are displayed in Supplementary Fig. 27a and Table 9. When integrated with the highly conductive Co-HHTP (80.12 ± 2.45 Ω $cm^{-2}$), NU-1000@Co-HHTP shows a lower charge transfer resistance ($R_{ct}$) of 65.23 ± 2.17 Ω $cm^{-2}$ than that of NU-1000 (179.80 ± 4.23 Ω $cm^{-2}$) and NU-1000/Co-HHTP (84.95 Ω±4.56 $cm^{-2}$), implying the stronger transport capability. In addition, the charge recombination behavior was then explored by open-circuit voltage decay (OCVD) measurements (Supplementary Figs. 26g and 27b). Compared to NU-1000, Co-HHTP and NU-1000/Co-HHTP, NU-1000@Co-HHTP affords higher open-circuit voltage under irradiation and slower photovoltage decay after the light is turned off, suggesting the slowest carrier recombination kinetics and longest photogenerated charge lifetime[56,57]. In the steady PL spectra (Supplementary Fig. 26h), NU-1000@Co-HHTP possesses the lowest fluorescence intensity with inhibited photogenerated electron-hole recombination. The charge carrier dynamics were further probed by time-resolved PL (TRPL) spectroscopy fitted with a biexponential function (Supplementary Fig. 26i). As seen, NU-1000@Co-HHTP exhibits an obviously longer average fluorescence lifetime of charge carriers (28.69 ns) than NU-1000 (6.31 ns), Co-HHTP (18.20 ns) and NU-1000/Co-HHTP (14.32 ns), demonstrating the longer-lived charge pairs in NU-1000@Co-HHTP. The improvements in charge transfer and separation also contributes to the enhanced photocatalytic efficiency of NU-1000@Co-HHTP.

To further understand the enhanced performance of NU-1000@Co-HHTP, density functional theory (DFT) calculations were performed. Density functional theory (DFT) calculations (Supplementary Data 1 and 2) were performed to support the experimental findings. The charge difference distribution diagram (Fig. 6a) shows the electron accumulation around the Zr atoms and electron depletion from the Co atoms, suggesting the electron transfer from NU-1000 to Co-HHTP, in accordance with the XPS and UPS results. Besides, the adsorption energies of $NO_3^-$ and $CO_2$ reactants on different sites for NU-1000, Co-HHTP and NU-1000@Co-HHTP were calculated (Fig. 6b and Supplementary Fig. 28). For Co-HHTP, the adsorption energy of $*NO_3^-$ on Co is -0.96 eV, significantly lower than that of $CO_2$ (-0.12 eV, Fig. 5b), suggesting the preferential $*NO_3^-$ adsorption on Co sites. In contrast for NU-1000, the $CO_2$ adsorption is more favorable on Zr sites, as supported by the lower adsorption energy of $CO_2$ (-0.37 eV) than $NO_3^-$ (-0.16 eV). Compared to Co-HHTP and NU-1000, the adsorption energies of $NO_3^-$ (-1.33 eV) on Co sites and $CO_2$ (-0.52 eV) on Zr sites are more negative, revealing the enhanced reactant adsorption within the heterostructure.

Furthermore, the Gibbs free energy change (ΔG) of each elementary step during the NitRR@CRR process are presented in Fig. 6c with the corresponding adsorption configurations illustrated in Supplementary Figs. 29 and 30. According to the S-scheme charge transfer mechanism, the Co centers serve as reduction sites within NU-1000@Co-HHTP. Therefore, the reaction pathway for urea synthesis was initiated from $NO_3^-$ reduction. As seen, the potential determination step (PDS) for NU-1000@Co-HHTP was recognized as the first C-N coupling step ($*NO + CO_2 \rightarrow *CO_2NO$) with ΔG of 0.2 eV, lower than that for Co-HHTP (0.58 eV). A similar trend is also found in the second C-N coupling step ($*CONH_2 + *NO \rightarrow *CONONH_2$) with ΔG of 0.15 and 0.44 eV for NU-1000@Co-HHTP and Co-HHTP, respectively. The observations suggest the promoted C-N coupling over NU-1000@Co-HHTP. To gain further insight into the C-N coupling step, the transition state (TS) profiles and optimized configurations of the PDS for the two samples are displayed in Figs. 6d, e and Supplementary Fig. 31. The energy barrier from *NO on Co site to TS ($\Delta G_{TS}$) via the coupling with $*CO_2$ on neighboring Zr site is calculated to be 0.3 eV for NU-1000@Co-HHTP, significantly lower than that for Co-HHTP (0.79 eV) that experiences the C-N coupling between *NO and free $CO_2$. Therefore, the coupling between *NO and $CO_2$ is kinetically more favorable over NU-1000@Co-HHTP with interfacial Zr-Co dual sites, facilitating the formation of C-N bonds toward boosted urea synthesis. Given the difficulties in modelling the exact structures under catalytic conditions using DFT calculations, the theoretical results primarily serve to support the experimental findings.

The experimental results with the aid of DFT calculations reveal the crucial role of MOF-on-MOF S-scheme heterojunction with interfacial dual sites in enhancing photocatalytic C-N coupling efficiency for urea synthesis. During the photocatalysis process, the Co sites within the NU-1000@Co-HHTP heterojunction are responsible for the adsorption and reduction of $NO_3^-$ to *NO intermediate. The adjacent Zr sites at the interface supply $CO_2$ for the C-N coupling with *NO on Co sites, reducing the energy barrier for the formation C-N intermediates (e.g., $*NOCO_2$ and $*CONONH_2$). For NU-1000 with single Zr sites and Co-HHTP with single Co sites, it is noted that the adsorption energy of either Zr or Co sites for both $CO_2$ and $NO_3^-$ adsorption is negative. Thus, the chance of urea formation via P-NitRR&CRR cannot be avoided, as evidenced by the formation of urea with a low yield in the two individual MOF catalysts. However, the adsorption energy of Co sites

https://doi.org/10.1038/s41467-026-69281-8

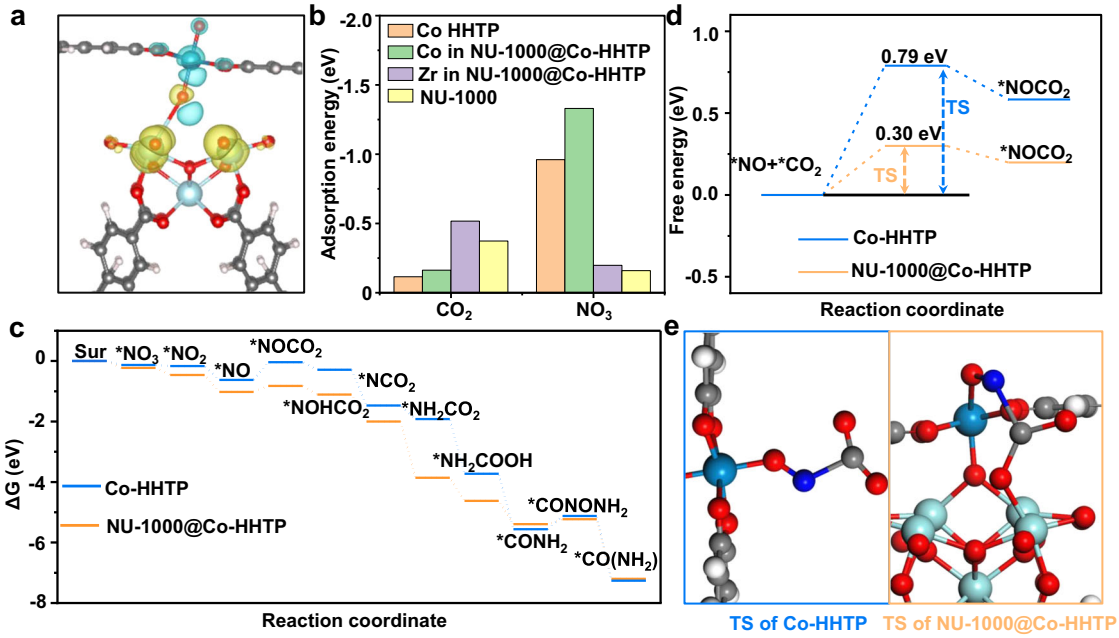


**Fig. 6 | DFT calculations. a** Calculated charge difference distribution of NU-1000@Co-HHTP (the yellow and blue regions refer to electron accumulation and depletion regions, respectively), **b** adsorption energy of $NO_3^-$ and $CO_2$ on the Zr and Co sites in Co-HHTP, NU-1000 and NU-1000@Co-HHTP, **c** Gibbs free energy diagram for NitRR&CRR on Co-HHTP and NU-1000@Co-HHTP, **d** energy barrier of coupling between *NO and $CO_2$ to $*CO_2NO$ for Co-HHTP and NU-1000@Co-HHTP, **e** optimized configurations of TS for Co-HHTP and NU-1000@Co-HHTP. Color code: Co, cyan; Zr, green; C, gray; N, blue; O, red; H, white. Source data for Fig. 6 are provided as a Source Data file.

in Co-HHTP for $CO_2$ is the highest among all test groups, the same is the $NO_3^-$ adsorption energy of Zr sites in NU-1000, in contrast to NU-1000@Co-HHTP that has the lowest adsorption energy for both $CO_2$ and $NO_3^-$ adsorption. Therefore, the overall performance of NU-1000 and Co-HHTP is significantly inferior than NU-1000@Co-HHTP. In addition, the S-scheme charge transfer pathway facilitates the electron-hole separation and offers strong redox capability. Collectively, the enhanced performance of urea photosynthesis is achieved.

## Discussion

In summary, a NU-1000@Co-HHTP MOF-on-MOF S-scheme heterojunction has been designed for efficient P-NitRR&CRR, exhibiting a high urea yield of 3523.4 $\mu g\ g^{-1}\ h^{-1}$ and an AQY of 1.16% at 365 nm in the absence of sacrificial agents. Our systematical investigations reveal that the formation of interfacial Co-Zr dual sites plays a crucial role in boosting C-N coupling. The Co sites reduce $NO_3^-$ to *NO intermediates, while the Zr sites supply $CO_2$ for C-N coupling with *NO on adjacent Co sites, cooperatively lowering the reaction barriers. Together with the efficient S-scheme charge separation by constructing S-scheme heterojunction, the improved P-NitRR&CRR performance is achieved. Our findings have provided new insights into the development of high performance photocatalysts for urea production.

## Methods

### Chemicals

Zirconyl chloride octahydrate ($ZrOCl_2{\cdot}8H_2O$, 98%), cobalt(II) acetate tetrahydrate ($Co(CH_3COO)_2{\cdot}4H_2O$, 99%), 4,4′,4″,4‴-(pyrene-1,3,6,8-tetrayl)tetrabenzoate ($H_4TBAPy$, 98%), 4-phenylbenzoic acid (98%), 2,3,6,7,10,11-hexahydroxytriphenylene (HHTP, 99%), ferric chloride anhydrous ($FeCl_3$, 99.99%), diacetylmonoxime (99%), thiosemicarbazide (99%), p-aminobenzenesulfonamide (99%), N-(1-naphthyl) ethylenediamine dihydrochloride (99%), N,N-dimethylformamide (DMF, 99.8%), 1-propanol ($C_3H_8O$, ≥95.0%), 1-propanol ($C_3H_8O$, ≥95.0%) and ethanol ($C_2H_5OH$, 99%) were purchased from Adamas-beta. Sodium hypochlorite solution (NaClO, 6-14%), potassium hydroxide (KOH, 96%), sodium hydroxide (NaOH, 96%), sodium salicylate ($C_7H_5O_3Na$, 99.5%) and sodium nitroferricyanide dehydrate ($C_5FeN_6Na_2O$, 99%) were purchased from Aladdin. Sodium citrate (98%), sulfuric acid, salicylic acid (99%), hydrochloric acid (36-38%), sulfuric acid (98%) and phosphoric acid (85%) were purchased from Sinopharm Chemical Reagent Co. Ltd. All the solutions used in the experiments were prepared by ultrapure water. All the materials were used as received without further purification.

### Synthesis of NU-1000

In a typical synthesis, 40 mg of $ZrOCl_2{\cdot}8H_2O$ and 1.8 g of 4-phenylbenzoic acid were dissolved in 5 mL of DMF in a vial. 10 mg of TBAPy was dissolved in 3 mL of DMF in another vial. The two vials were heated at 90 °C for 1 h. After cooling down to room temperature, the two solutions were mixed by sonication treatment for 10 min. The resultant suspension was then heated at 120 °C for 1 h. Finally, the products were collected by centrifugation, washed with DMF and dried at 55 °C for further use.

### Synthesis of NU-1000@Co-HHTP

5 mg of NU-1000 was dispersed into a mixture solution containing 4 mL of 1-propanol and 3.5 mg of HHTP by sonication for 20 min. Subsequently, 4 mL of $Co(CH_3COO)_2{\cdot}4H_2O$ aqueous solution (0.8 mg $mL^{-1}$) was poured into the above suspension. By further heating at 55 °C for 2 h, the final products were collected by centrifugation, washed with $H_2O$ and ethanol for three times and dried overnight.

### Synthesis of Co-HHTP

Co-HHTP nanorods were prepared by using the similar synthesis process of NU-1000@Co-HHTP except without the addition of NU-1000.

### Material characterization

Scanning electron microscopy (SEM) images were collected by scanning electron microscope (HITACHI-S4800). Transmission electron

microscopy (TEM) were performed on a JEOL 2100 F instrument at 200 KV. A field-emission scanning electron microscope (Helios G4 UX, FEI Inc. USA) equipped with a focused ion beam (FIB) system and an energy-dispersive X-ray spectroscopy (EDS) detector (X-Max 150 T, Oxford Instruments, UK) was used to probe the elemental distribution. X-ray diffraction (XRD) patterns were acquired on a diffractometer (Bruker D8 Advanced) equipped with Cu Kα X-ray source (λ = 0.154 nm). X-ray photoelectron spectroscopy (XPS) tests were carried out on a PHI Quantera II ESCA instrument by using Al Kα radiation (1486.8 eV). The concentrations of metal ions were measured by Agilent 730 inductively coupled plasma-optical emission spectrometry (ICP-OES). Diffuse reflectance UV-vis absorption spectroscopy was recorded on a UV-vis spectrophotometer (Lambda 950). $N_2$ sorption measurements and $CO_2$ adsorption were performed on a Micromeritics ASAP-2460 at 77 K and 273 K, respectively. The samples were degassed in vacuum at 423 K for 24 h before analysis. The temperature-programmed desorption of $CO_2$ ($CO_2$-TPD) was carried out on a Micromeritics Chemisorb 2750. Ultraviolet photoelectron spectroscopy (UPS) measurements were carried out on an ESCALAB 250 XI setup by using a monochromatic He (21.22 eV) radiation source. PL spectra were recorded on an Edinburgh FS5 spectrofluorometer. Time-resolved photoluminescence (TRPL) spectra were collected on a FSL980 transient fluorescence spectrometer. FTIR spectra were recorded on a Nicolet Fourier spectrophotometer using KBr pellets. A nuclear magnetic resonance (NMR) spectrometer (600 MHz $^1$H NMR, Bruker AVANCE III HD) was used to quantify urea and ammonia concentration.

### Evaluation of photocatalytic activity

Typically, 20 mg of photocatalyst was dispersed in 40 mL of $KNO_3$ (1 M) by ultrasonication for 10 min. After continuously bubbled with $CO_2$ for 30 min to remove air residual, a 300 W xenon lamp (PLS-SXE300D/300DUV, Perfect Light) was used as the visible light source (λ > 400 nm) with a light intensity of 100 mW cm$^{-2}$ to initiate the reaction. The photocatalytic reaction was conducted for 4 h under stirring at 600 rpm and the temperature of the reaction solution was kept at 25 °C by an external circulating cooling water system. Throughout the reaction, 1 mL of reaction solution was collected at regular time intervals (1 h) and filtrated with 0.22 μm filters to remove the photocatalysts for quantitative analysis. The produced urea in the reaction solution was quantified by diacetylmonoxime-thiosemicarbazide (DAMO-TSC) and NMR methods, respectively. All error bars of the results were derived from three independent replicate experiments.

### Calculation methods for apparent quantum yield (AQY)

To calculate the AQY, the incident light was passed through a monochromator with the bandpass filter at wavelengths of 365 nm, 400 nm, 450 nm, 500 nm, 550 nm, 600 nm, and 650 nm as the light source, respectively. In addition, an optical power meter (PL-MW2000, Beijing Perfectlight Technology) was utilized to detect the light intensity. The errors of urea yield represent the standard deviations of three independent measurements. The AQY was calculated by the following equation:

$$\begin{aligned} \mathrm{AQY}(\%) &= \frac{\mathrm{numberofreactedelectrons}}{\mathrm{numberofincidentphotons}} \times 100\% \\ &= \frac{\mathrm{numberofevolvedureamolecules} \times 16}{\mathrm{numberofincidentphotons}} \times 100\%. \end{aligned} \quad (1)$$

### Determination of product concentration

**Determination of $H_2$, $N_2$ and CO.** The gas products were detected by gas chromatograph (Agilent 8860 GC).

**Urea quantification by DAMO-TSC method.** Firstly, 500 mg of diacetylmonoxime and 10 mg of thiosemicarbazide were dissolved in 100 mL of $H_2O$ to prepare reagent A, and 10 mL of $H_3PO_4$, 30 mL of $H_2SO_4$, and 10 mg of $FeCl_3$ were dissolved in 60 mL of $H_2O$ to prepared reagent B. Afterwards, 1 mL of the reaction solution was collected by mixing 1 mL of reagent A and 2 mL of reagent B. After reacting in a boiling water bath at 100 °C for 20 min, the absorbance of the mixture solution was determined by UV-vis spectrophotometer at 655 nm for quantifying the urea concentration according to the standard calibration curve.

$^1$H NMR measurement was also conducted to quantitatively detect urea. 5 mL of the reaction solution was collected, concentrated via rotary evaporation, and subsequently redissolved in a mixture containing 500 μL of DMOS solution, 50 μL of DMSO-$d_6$ and 20 μL of maleic acid (1 ppm). The resulting solution was transferred to an NMR tube for analysis.

**Determination of $NO_2^-$.** The mixed solution of p-aminobenzenesulfonamide (4 g), N-(1-naphthyl) ethylenediamine dihydrochloride (0.2 g), DI water (50 mL) and phosphoric acid (10 mL) was used as the color reagent. 200 μL of reaction solution was mixed with 0.1 mL of color reagent. After sitting for 20 min, the absorption intensity of the solution was measured by a UV-vis spectrophotometer at a wavelength of 540 nm. The concentration of $NO_2^-$ was then quantified according to the standard curve (Supplementary Fig. 16)[40].

**Determination of $NH_3$.** The concentration of ammonia product was measured by NMR. 5 mL of 0.1 M HCl, 50 μL of $D_2O$ and 5 mL of maleic acid (50 ppm, an internal standard solution) were added into 5 mL of the diluted reaction solution. Afterwards, the concentration of generated $NH_3$ was determined by NMR according to the standard curve (Supplementary Fig. 17)[40].

### Photoelectrochemical test

Photoelectrochemical measurements were performed on a Chenhua CHI 760E electrochemical workstation in 0.1 M $Na_2SO_4$ electrolyte (pH = 7 ± 0.2). A typical three-electrode setup was employed, consisting of a Pt wire counter electrode, an Ag/AgCl reference electrode, and a working electrode made from photocatalyst-modified indium tin oxide (ITO). The detailed procedure for preparing working electrode was as follows: 20 mg of the catalysts was first dispersed in 60 μL of a 10% Nafion solution. The resultant slurry was then drop-casted onto a 1 cm$^2$ area of ITO glass and dried at 55 °C overnight. To record photocurrent signals, a 300 W xenon lamp (PLS Light, model SXE300D/300DUV) was used as the light source. EIS measurements were performed using an AC perturbation signal of 10 mV over a frequency range of 0.1-10$^5$ Hz. Mott-Schottky plots were examined with a scan rate of 5 mV s$^{-1}$ at 500 Hz and 1500 Hz. During the transient open-circuit voltage decay (OCVD) tests for 800 s, the visible-light source was switched on and off with a time interval of 300 s. The average carrier lifetimes ($\tau_n$) were determined from the open-circuit voltage ($V_{oc}$) decay using the following formula:

$$\tau_n = -\frac{k_B T}{q}\left(\frac{dV_{oc}}{dt}\right)^{-1} \quad (2)$$

where $\tau_n$ represents the average lifetime, $V_{oc}$ is open-circuit voltage, $k_B$ is the Boltzmann constant, $T$ is the temperature (in Kelvin), and $q$ is the unsigned charge of an electron.

The flat-band potential values are determined using the Mott-Schottky equation:

$$\frac{1}{C^2} = \frac{2}{\varepsilon_0 \varepsilon N_D}\left(E - E_{fb} - \frac{T\kappa_B}{q}\right) \quad (3)$$

where C is the space charge capacitance, $N_D$ is the donor density, ε and $\varepsilon_0$ are the dielectric constants of free space and the film electrode, respectively, E is the applied potential, $E_{fb}$ is the flat-band potential, $\kappa_B$ is Boltzmann constant, T is the temperature, and q is the electronic charge. The $E_{fb}$ value can be determined from the extrapolation to $1/C^2 = 0$. For n-type semiconductors, the conduction bands are 0.1 eV higher than the flat potentials. All the potentials were calibrated with a reversible hydrogen electrode (RHE)

$$E_{RHE} = E_{Ag/AgCl} + 0.0591 \times pH + 0.197 \quad (4)$$

All the electrochemical tests were performed without IR compensation.

### In situ diffuse reflectance infrared Fourier transform spectroscopy measurements

40 mg of photocatalyst was vigorously stirred in 25 mL of 1.0 M $KNO_3$ solution for 6 h, followed by centrifugation and drying at 55 °C for 12 h. Afterwards, 25 mg of the $NO_3^-$ adsorbed catalyst was placed in a diffuse reflectance cell at room temperature with continuous $CO_2$ (99.999%) purging. The time-dependent FTIR profiles were then recorded under 300 W Xeon lamp irradiation.

### Computational details

Vienna Ab initio Simulation Package (VASP) was employed to perform the Spin-polarized density functional theory (DFT) calculations[58,59]. The generalized gradient approximation (GGA) in combination with the Perdew–Burke–Ernzerhof (PBE) functional was used to describe the exchange–correlation interactions[60]. In addition, the relation between ionic cores and valence electrons was modeled using the projected augmented wave (PAW) method[61,62], and the electronic wave functions were expanded in a plane-wave basis set with a kinetic energy cutoff of 500 eV. Gaussian smearing approach with a width of 0.05 eV was applied to simulate the partial occupancies of the Kohn-Sham orbitals. Structural optimizations were conducted until the total energy and force converged to within $10^{-5}$ eV and 0.02 eV/Å, respectively. The initial models were built according to the standard crystal structures of NU-1000 and Co-HHTP. To minimize undesired periodic interactions, a vacuum layer of 18 Å was introduced along the direction normal to the material plane. For Brillouin-zone sampling during relaxation and self-consistent calculations, a 2 × 1 × 1 Monkhorst–Pack k-point mesh was employed[63]. The adsorption energies ($E_{ads}$) of reactants and intermediates were determined according to the formula of $E_{ads} = E_{ad/sub} - E_{ad} - E_{sub}$, where $E_{ad/sub}$, $E_{ad}$, and $E_{sub}$ refer to the total energies of optimized adsorption configuration, individual adsorbate and substrate, respectively. Besides, the Gibbs free energy (G) was determined based on the equation:

$$G = E + ZPE - TS \quad (5)$$

where E is the total energy, ZPE refers to the zero-point energy, and TS represents the entropic contributions.

## Data availability

The raw data generated in this study are provided in the Supplementary Information. All data are available from the corresponding author upon request. Source data are provided with this paper.

## References


1. Li, J. et al. Construction of C–N bonds from small-molecule precursors through heterogeneous electrocatalysis. *Nat. Rev. Chem.* **6**, 303–319 (2022).
2. Liu, X. et al. Mechanism of C-N bonds formation in electrocatalytic urea production revealed by ab initio molecular dynamics simulation. *Nat. Commun.* **13**, 5471 (2022).
3. Xu, M. et al. Kinetically matched C–N coupling toward efficient urea electrosynthesis enabled on copper single-atom alloy. *Nat. Commun.* **14**, 6994 (2023).
4. MacFarlane, D. R. et al. A roadmap to the ammonia economy. *Joule* **4**, 1186–1205 (2020).
5. Lv, C. et al. Selective electrocatalytic synthesis of urea with nitrate and carbon dioxide. *Nat. Sustain.* **4**, 868–876 (2021).
6. Chen, K. et al. Urea electrosynthesis from nitrate and $CO_2$ on diatomic alloys. *Adv. Mater.* **36**, 2402160 (2024).
7. Lv, Z. et al. Coactivation of multiphase reactants for the electrosynthesis of urea. *Adv. Energy Mater.* **13**, 2300946 (2023).
8. Shi, C. et al. Nitric acid-mediated artificial urea photo-synthesis with $N_2$ and $CO_2$. *Adv. Energy Mater.* **14**, 2400201 (2024).
9. Wang, Y., Chen, D., Chen, C. & Wang, S. Electrocatalytic urea synthesis via C–N coupling from $CO_2$ and nitrogenous species. *Acc. Chem. Res.* **57**, 247–256 (2023).
10. Yang, S. et al. Photocatalytic co-reduction of $N_2$ and $CO_2$ with $CeO_2$ catalyst for urea synthesis. *Angew. Chem. Int. Ed.* **62**, e202312076 (2023).
11. Ahmad, M. I. et al. Enhanced photocatalytic synthesis of urea from co-reduction of $N_2$ and $CO_2$ on Z-schematic $SrTiO_3$-FeS-$CoWO_4$ heterostructure. *Angew. Chem. Int. Ed.* **64**, e202419628 (2024).
12. Wei, X. et al. Oxygen vacancy-mediated selective C–N coupling toward electrocatalytic urea synthesis. *J. Am. Chem. Soc.* **144**, 11530–11535 (2022).
13. Sun, H. et al. Enhanced solar urea synthesis from $CO_2$ and nitrate waste via oxygen vacancy mediated-$TiO_x$ support lead-free perovskite. *Appl. Catal. B-Environ.* **360**, 124511 (2025).
14. Wang, Z. et al. Orderly coating of bilayer polymer to tailor microenvironment for efficient C-N coupling toward highly selective urea electrosynthesis. *Angew. Chem. Int. Ed.* **64**, e202416832 (2024).
15. Carvalho, O. Q. et al. Role of electronic structure on nitrate reduction to ammonium: A periodic journey. *J. Am. Chem. Soc.* **144**, 14809–14818 (2022).
16. Chen, X. et al. Amorphous bismuth–tin oxide nanosheets with optimized C-N coupling for efficient urea synthesis. *J. Am. Chem. Soc.* **146**, 13527–13535 (2024).
17. Jiao, Y. et al. Activity and selectivity roadmap for C–N electrocoupling on mxenes. *J. Am. Chem. Soc.* **145**, 15572–15580 (2023).
18. Xi, Y. et al. Modulating active hydrogen supply and $O_2$ adsorption: sulfur vacancy matters for boosting $H_2O_2$ photosynthesis performance. *Angew. Chem. Int. Ed.* **64**, e202505046, (2025).
19. Yuan, L. et al. Nanoporous heterojunction photocatalysts with engineered interfacial sites for efficient photocatalytic nitrogen fixation. *Angew. Chem. Int. Ed.* **63**, e202412340 (2024).
20. Huang, Q. P. et al. Building ultrathin MOL/MOL S-Scheme heterostructures toward boosted photocatalytic charge kinetics for efficient $H_2$ evolution. *Angew. Chem. Int. Ed.* **64**, e202502009 (2025).
21. Jin, R. et al. Beyond tradition: a MOF-on-MOF cascade Z-Scheme heterostructure for augmented $CO_2$ photoreduction. *Small* 10, 2409759, (2025).
22. Yuan, L. et al. A S-scheme MOF-on-MOF heterostructure. *Adv. Funct. Mater.* **33**, 2214627 (2023).
23. Abazari, R. et al. Design and advanced manufacturing of NU-1000 metal–organic frameworks with future perspectives for environmental and renewable energy applications. *Small* **20**, 2306353 (2023).
24. Mondloch, J. E. et al. Vapor-phase metalation by atomic layer deposition in a metal–organic framework. *J. Am. Chem. Soc.* **135**, 10294–10297 (2013).
25. Zou, Y. et al. MOF-on-MOF heterostructured electrocatalysts for efficient nitrate reduction to ammonia. *Angew. Chem. Int. Ed.* **63**, e202409799 (2024).
26. Liu, Y. et al. Face-to-face growth of wafer-scale 2D semiconducting MOF films on dielectric substrates. *Adv. Mater.* **33**, 2007741 (2021).

27. Hmadeh, M. et al. New porous crystals of extended metal-catecholates. *Chem. Mater.* **24**, 3511–3513 (2012).
28. Mercuri, G. et al. Temperature-dependent nitrous oxide/carbon dioxide preferential adsorption in a thiazolium-functionalized NU-1000 metal–organic framework. *ACS Appl. Mater. Interfaces* **13**, 58982–58993 (2021).
29. Liu, L. et al. A novel hexagonal prism of Zr-based MOF@$ZnIn_2S_4$ core–shell nanorod as an efficient photocatalyst for hydrogen evolution. *Appl. Catal. B-Environ.* **361**, 124686 (2025).
30. Gu, M. et al. Unveiling charge carrier dynamics at organic–inorganic S-Scheme heterojunction interfaces: insights from advanced EPR. *Adv. Mater.* **37**, 2414803 (2024).
31. Bao, T. et al. Highly efficient nitrogen fixation over S-scheme heterojunction photocatalysts with enhanced active hydrogen supply. *Natl. Sci. Rev.* **11**, nwae093 (2024).
32. Zhao, Q.-Y. et al. Ag-bridged Z-Scheme AgI/NU-1000 heterojunction for enhanced photocatalytic degradation of sulfamethazine: pathways, mechanism insight, and DFT calculations. *Sep. Purif. Technol.* **354**, 128875 (2025).
33. Wang, X. et al. Interfacial chemical bond and internal electric field modulated Z-Scheme Sv-$ZnIn_2S_4$/$MoSe_2$ photocatalyst for efficient hydrogen evolution. *Nat. Commun.* **12**, 4112 (2021).
34. Meng, Z. et al. Kelvin probe force microscopy reveals spatially resolved charge-transfer mechanism in CdS/BiOBr S-scheme heterojunction photocatalyst. *Angew. Chem. Int. Ed.* **64**, e202505456 (2025).
35. Wang, Y. et al. Photocatalytic coreduction of $N_2$ and $CO_2$ with $H_2O$ to $(NH_2)_2CO$ on 2D-CdS/3D-BiOBr. *ACS Sustain. Chem. Eng.* **11**, 1962–1973 (2023).
36. Li, D. et al. Accelerating electron-transfer dynamics by $TiO_2$-immobilized reversible single-atom copper for enhanced artificial photosynthesis of urea. *Adv. Mater.* **34**, 2207793 (2022).
37. Zhang, Y. et al. Synergy of photogenerated electrons and holes toward efficient photocatalytic urea synthesis from $CO_2$ and $N_2$. *Angew. Chem. Int. Ed.* **63**, e202405637 (2024).
38. Yang, S. et al. Photocatalytic C–N coupling towards urea synthesis with a palladium-supported $CeO_2$ catalyst. *Catal. Sci. Technol.* **13**, 1855–1865 (2023).
39. Wang, Y. et al. Direct and indirect Z-Scheme heterostructure-coupled photosystem enabling cooperation of $CO_2$ reduction and $H_2O$ oxidation. *Nat. Commun.* **11**, 3043 (2020).
40. Xi, Y. et al. Nanoarchitectonics of S-Scheme heterojunction photocatalysts: a nanohouse design improves photocatalytic nitrate reduction to ammonia performance. *Angew. Chem. Int. Ed.* **63**, e202409163 (2024).
41. Bao, T. et al. Photocatalytic co-reduction of $CO_2$ and nitrate over porphyrin metal–organic frameworks: dual atomic active site and nanostructure synergy enhances C–N coupling for urea production. *Angew. Chem. Int. Ed.* **64**, e202512615 (2025).
42. Zhu, Z. et al. High-capacity, cooperative $CO_2$ capture in a diamine-appended metal–organic framework through a combined chemisorptive and physisorptive mechanism. *J. Am. Chem. Soc.* **146**, 6072–6083 (2024).
43. Zhang, D., Xue, Y., Zheng, X., Zhang, C. & Li, Y. Multi-heterointerfaces for selective and efficient urea production. *Natl. Sci. Rev.* **10**, nwac209 (2023).
44. Zhan, P. et al. Efficient electrosynthesis of urea over single-atom alloy with electronic metal support interaction. *Angew. Chem. Int. Ed.* **63**, e202409019 (2024).
45. Zhang, X. et al. Dynamic control of asymmetric charge distribution for electrocatalytic urea synthesis. *Adv. Mater.* **36**, 2408510 (2024).
46. Du, W. et al. Synergistic Cu single atoms and $MoS_2$-edges for tandem electrocatalytic reduction of $NO_3^-$ and $CO_2$ to Urea. *Adv. Energy Mater.* **14**, 2401765 (2024).
47. Sun, M. et al. Carbon-anchored molybdenum oxide nanoclusters as efficient catalysts for the electrosynthesis of ammonia and urea. *Angew. Chem. Int. Ed.* **62**, e202301957 (2023).
48. Qiu, X. F. et al. Highly efficient electrosynthesis of urea from $CO_2$ and nitrate by a metal–organic framework with dual active sites. *Angew. Chem. Int. Ed.* **63**, e202410625 (2024).
49. Qian, G. et al. Efficient photoreduction of diluted $CO_2$ to tunable syngas by Ni–Co dual sites through d-band center manipulation. *Angew. Chem. Int. Ed.* **61**, e202210576 (2022).
50. Yang, Y. et al. Electronic structure tuning in Cu–Co dual single atom catalysts for enhanced COOH* spillover and electrocalytic $CO_2$ reduction activity. *Angew. Chem. Int. Ed.* **64**, e202504423 (2025).
51. Huang, X. et al. A versatile strategy for broadening light absorption to ultraviolet–visible region on Zr-based MOF photocatalysts for efficient $CO_2$ reduction. *Chem. Eng. J.* **507**, 160812 (2025).
52. Li, J. et al. Subnanometric alkaline-earth oxide clusters for sustainable nitrate to ammonia photosynthesis. *Nat. Commun.* **13**, 1098 (2022).
53. Li, P. et al. Visible-light-driven nitrogen fixation catalyzed by $Bi_5O_7Br$ nanostructures: enhanced performance by oxygen vacancies. *J. Am. Chem. Soc.* **142**, 12430–12439 (2020).
54. Huang, X. et al. The tandem nitrate and $CO_2$ reduction for urea electrosynthesis: role of surface n-intermediates in $CO_2$ capture and activation. *Angew. Chem. Int. Ed.* **63**, e202403980 (2024).
55. Song, X. et al. Boosting urea electrosynthesis via asymmetric oxygen vacancies in Zn-Doped $Fe_2O_3$ catalysts. *Angew. Chem. Int. Ed.* **64**, e202501830 (2025).
56. Wang, M. et al. Triple-phase boundaries enable selective urea production from simulated flue gas in a zero-gap electrolyzer. *Angew. Chem. Int. Ed.* **64**, e202505987 (2025).
57. Gao, Y. et al. Regulating charge separation via periodic array nanostructures for plasmon-enhanced water oxidation. *Adv. Mater.* **37**, 2414959 (2024).
58. Kresse, G. et al. Efficiency of ab-initio total energy calculations for metals and semiconductors using a plane-wave basis set. *Comput. Mater. Sci.* **6**, 15–50 (1996).
59. Kresse, G. et al. Efficient iterative schemes for ab initio total-energy calculations using a plane-wave basis set,. *Phys. Rev. B* **54**, 11169–11186 (1996).
60. Perdew, J. P. et al. Generalized gradient approximation made simple. *Phys. Rev. Lett.* **77**, 3865–3868 (1996).
61. Kresse, G. et al. From ultrasoft pseudopotentials to the projector augmented-wave method. *Phys. Rev. B* **59**, 1758–1775 (1999).
62. Blöchl, P. E. Projector augmented-wave method. *Phys. Rev. B* **50**, 17953–17979 (1994).
63. Monkhorst, H. J. et al. Special points for Brillouin-zone integrations. *Phys. Rev. B* **13**, 5188–5192 (1976).


## Acknowledgements

The authors acknowledge support from the National Natural Science Foundation of China (Grant No. 22475072, 22075085 and 22572056), the Natural Science Foundation of Shanghai (25ZR1402122), the Shanghai Frontiers Science Center of Molecule Intelligent Syntheses and the Fundamental Research Funds for the Central Universities. East China Normal University Multifunctional Platform for Innovation (004).

## Author contributions

Y.X., C.Y., and C.L. conceived the idea. T.B. and S.L. performed most of material synthesis and characterizations and photochemical measurements. T.W., W.T., Y.G., and Y.Z. took part in the photocatalytic measurements and discussions. C.Z. carried out the DFT calculations. C.Y. and C.L. supervised the work and directed the research. All authors were involved in the discussions and reviewed the manuscript.

## Competing interests
The authors declare no competing interests.

## Additional information
**Supplementary information** The online version contains supplementary material available at https://doi.org/10.1038/s41467-026-69281-8.

**Correspondence** and requests for materials should be addressed to Chao Liu.

**Peer review information** *Nature Communications* thanks Dingsheng Wang and the other anonymous, reviewer(s) for their contribution to the peer review of this work. A peer review file is available.